

Single- and double-slit electron diffraction in an anisotropic two-dimensional medium


F. R. V. Araújo^{1,*}, D. R. da Costa^{2,3,*}, F. S. L. da Silva¹, I. V. de Sousa, Jr.⁴ and J. M. Pereira, Jr.^{2,§}

¹*Campus Piripiri, Instituto Federal de Educação, Ciência e Tecnologia do Piauí, 64260-000, Piripiri, PI, Brazil*

²*Departamento de Física, Universidade Federal do Ceará, 60455-900, Fortaleza, CE, Brazil*

³*Department of Physics, University of Antwerp, Groenenborgerlaan 171, B-2020 Antwerp, Belgium*

⁴*Campus Parnaíba, Instituto Federal de Educação, Ciência e Tecnologia do Piauí, 64211-145, Parnaíba, PI, Brazil*

 (Received 4 March 2024; revised 7 August 2024; accepted 12 August 2024; published 22 August 2024)

We theoretically investigate the effect of anisotropy on electron diffraction in two-dimensional (2D) systems. The calculations are performed by means of both analytical semiclassical and microscopic tight-binding approaches, with the anisotropy being introduced by assuming direction-dependent effective masses and hoppings, respectively. Single and double slits with different orientations with respect to the anisotropy axis are considered. Using these models, we obtain analytical expressions for the wave function and numerical results for the probability current density for both investigated cases. In addition, we specify the conditions under which there is constructive or destructive interference in the interference pattern in the double-slit case. The results show that anisotropy can lead to a collimation effect, as well as a steering of the diffracted electronic beam, which may, in turn, allow the control of the charge carriers' propagation to be used in nanoelectronic devices based on anisotropic 2D media systems.

DOI: [10.1103/PhysRevB.110.085424](https://doi.org/10.1103/PhysRevB.110.085424)

I. INTRODUCTION

One of the early triumphs of quantum mechanics was the development of band theory to explain the electronic properties of crystals. A striking aspect of that theory is the fact that electrons (and holes) interacting with the periodic potential of the crystal are described as effectively free particles, albeit with a modified mass. For solid-state structures with dimensions comparable to the mean-free path of charge carriers (i.e., in the ballistic regime), the wave aspect of the carriers becomes prominent, as evidenced by the fact that correct treatment of transport in that regime must take into account effects such as interference and diffraction [1,2]. Ballistic transport of electrons and holes has also been considered in the context of two-dimensional (2D) materials such as graphene [3–7], silicene [8,9], and others, especially since the mean-free path of carriers in these systems can often reach the micrometer range. Therefore, many phenomena usually associated with optics can now be implemented in electronic systems, and it becomes meaningful to apply an optical-electronic analogy to describe their dynamical properties [10–15]. On the other hand, the fact that electrons and holes, in contrast with photons, are massive charged fermions can lead to significant deviations from their optical counterparts, particularly their response to external electric and magnetic fields.

Among the variety of 2D materials that have been studied recently, some, such as phosphorene [16], arsenene [17], and

some transition metal dichalcogenides, for instance, ReS₂, ReSe₂, and TiS₃ [18–24], display anisotropic properties. An outstanding issue is then the possible influence of anisotropy on the ballistic transport in these systems and on wavelike phenomena such as diffraction and interference [25,26]. One way to tackle that is to consider the effect of a preferred direction on the electron diffraction patterns in nanostructures of anisotropic materials. Of particular interest is the possibility of exploiting the results in device applications that make use of optical analogies [27–32]. In particular, the fact that the anisotropy of the system implies a preferred direction can naturally lead one to question how the alignment of the system in relation to such direction can influence the propagation of charge carriers. Here, we show that the anisotropy can significantly influence both single- and double-slit electron diffraction, resulting in effects such as beam steering and self-collimation, which in turn are strongly dependent on the alignment of the setup with respect to the anisotropy axes.

Diffraction is a wave phenomenon that occurs when a wave of wavelength λ passes through an obstacle or a slit of size $\sim \lambda$ and is deflected in various directions. The longer the wavelength relative to the dimensions of the slit or obstacle, the stronger the diffraction effects. Diffraction can occur from one or more diffracting objects. For the case of a single slit of width a present in a wall far enough from a screen [see sketch in Fig. 1(a)], regions of minima are observed in the screen whenever $a \sin \theta = m\lambda$, where θ is the angular direction of propagation with respect to the center of the slit and $m = 1, 2, 3, \dots$. The intensity, in turn, is proportional to $(\sin \gamma / \gamma)^2$, where $\gamma = \pi a \sin \theta / \lambda$. In addition, in the case of double-slit [see sketch in Fig. 1(b)], the analysis is performed considering two walls and a screen: on the first wall, there is a slit through which a wave is diffracted; on the second wall,

*These authors contributed equally to this work.

†Contact author: ronan.viana@ifpi.edu.br

‡Contact author: diego_rabelo@fisica.ufc.br

§Contact author: pereira@fisica.ufc.br

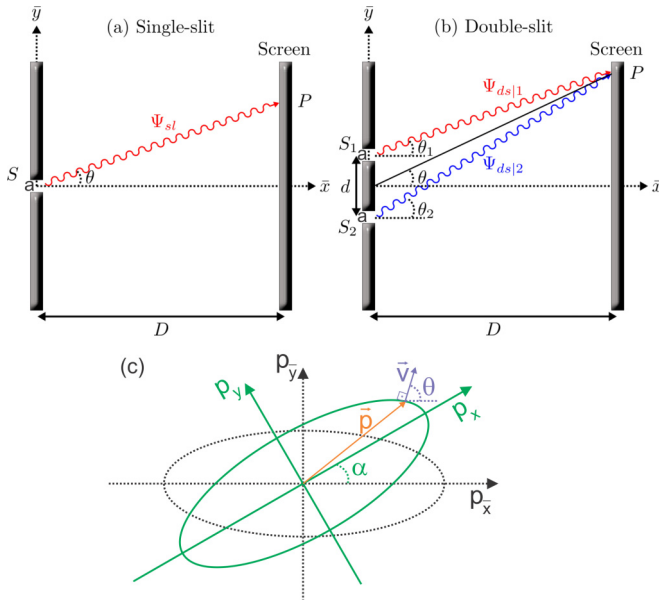


FIG. 1. Schematic illustrations of the (a) single- and (b) double-slit experiments theoretically studied in this work. In (a), a plane wave Ψ_{sl} coming from the slit S with width a forms an angle θ with the \bar{x} axis. In (b), two plane waves Ψ_{ds1} and Ψ_{ds2} emitted by slits S_1 and S_2 , separated by a distance d and widths a , form angles θ_1 and θ_2 with the \bar{x} axis, respectively. The plane waves in (a) and (b) reach the P point on the screen located at $\bar{x} = D$ and generate a specific pattern. The assumed system is anisotropic, i.e., with direction-dependent effective masses, and, consequently, exhibiting elliptical curves of constant energy in momentum space as depicted in (c). α is the rotation angle between the coordinate systems \bar{S} , aligned with the crystallographic axes (\bar{x} and \bar{y}) of the anisotropic 2D system, and S . Sketches in (a) and (b) illustrate the $\alpha = 0$ case slit experiments.

there are two slits separated by a distance d through which the wave diffracted by the previous wall gives rise to two waves and the screen is used to project the pattern formed by mixing both diffraction and interference effects. Despite being a well-established phenomenon described in detail both for light and for particles such as electrons in many textbooks [33,34], it has been the subject of several relatively recent studies, such as the diffraction of massive molecules through a single, a double, and a triple slit [35], obtaining the exact analytical values of the position and momentum information entropies for the single-slit and double-slit diffraction experiments [36], the electronic double-slit diffraction with a quantum mechanical approach [37], the proposal of a time-domain version of the double-slit experiment [38], obtaining single- and double-slit diffraction patterns by means of path integrals [39], in addition to the full modern realization of the experiment itself [40].

Although previous works have addressed some properties related to the analogy between optical and electronic transport of anisotropic 2D systems [41–49], to our knowledge, no investigation on the electronic diffraction for single and double slits defined in an anisotropic 2D system has been carried out on the electron optics' point of view as we performed here. For that, we explore the influence of the anisotropy on the wave function and, consequently, the probability density through an analytical semiclassical approach and the probability current

density through a quantum numerical description, where the anisotropy is introduced by assuming a direction-dependent effective mass and hopping energies.

The paper is organized as follows. Section II presents both the semiclassical approach (Sec. II A), where we analytically describe the investigated anisotropic 2D system and obtain expressions for the momenta along the x and y directions as a function of the effective masses for any crystallographic setup orientation, which will allow further to conveniently treat the single- and double-slit cases, and the quantum approach based on the tight-binding model (Sec. II B), whose numerical results for the probability current density will confirm our semiclassical calculations. Results for the single- and double-slit cases are discussed in Secs. III A and III B, respectively. A brief summary and final considerations are presented in Sec. IV.

II. ANISOTROPIC 2D MEDIA

A. Effective mass approach

Before discussing the electron optics of single- and double-slit anisotropic 2D systems, let us present the analytical model for anisotropic semiclassical systems, taking as a starting point an effective mass model, in which the anisotropy is introduced by assuming direction-dependent effective masses m_x and m_y [26]. Thus, the Hamiltonian \mathcal{H} has the form

$$\mathcal{H} = \frac{p_x^2}{2m_x} + \frac{p_y^2}{2m_y}, \quad (1)$$

where p_q and m_q , with $q = \{x, y\}$, are the momentum and the effective masses in the coordinate system \bar{S} , respectively, and the isoenergies in momentum space for this system exhibit an elliptical shape. To make it more general, it is convenient to consider another coordinate system S not parallel to the anisotropy axes, but rather rotated by an angle α counterclockwise with respect to the coordinate system \bar{S} , as illustrated in Fig. 1(c), resulting in $p_{\bar{x}} = p_x \cos \alpha - p_y \sin \alpha$ and $p_{\bar{y}} = p_x \sin \alpha + p_y \cos \alpha$, and also in a rotation of the elliptical constant energy curve by the angle α [see green solid curve in Fig. 1(c)]. Hence, the Hamiltonian (1) in the rotated coordinate system can be written as

$$\mathcal{H} = \frac{p_x^2}{2\mu_x} + \frac{p_y^2}{2\mu_y} + \frac{p_x p_y}{\mu}, \quad (2)$$

where

$$\frac{1}{\mu_{x(y)}} = \frac{\cos^2 \alpha}{m_{x(y)}} + \frac{\sin^2 \alpha}{m_{y(x)}} \quad (3)$$

and

$$\frac{1}{\mu} = \left[\frac{1}{m_y} - \frac{1}{m_x} \right] \sin \alpha \cos \alpha. \quad (4)$$

The velocity operator v_q is given by $v_q = \frac{\partial \mathcal{H}}{\partial p_q}$. Thus, from that definition and Eq. (2), we can specify the dependency between v_q and p_q as

$$v_x = \frac{p_x}{\mu_x} + \frac{p_y}{\mu}, \quad (5a)$$

$$v_y = \frac{p_x}{\mu} + \frac{p_y}{\mu_y}. \quad (5b)$$

One can then obtain the relation between the momentum and velocity components as

$$p_{x(y)} = \frac{v}{\rho} f_{x(y)}(\theta), \quad (6)$$

where $\rho \equiv 1 - \mu_x \mu_y / \mu^2 \neq 0$, $\mathbf{v} = v(\cos \theta, \sin \theta)$ is the velocity vector perpendicular to the elliptical isoenergy, as shown in Fig. 1(c), and the angle-dependent functions $f_{x,y}$ are given by

$$f_x(\theta) \equiv \mu_x \cos \theta - \frac{\mu_x \mu_y}{\mu} \sin \theta, \quad (7a)$$

$$f_y(\theta) \equiv \mu_y \sin \theta - \frac{\mu_x \mu_y}{\mu} \cos \theta. \quad (7b)$$

Equation (6) is written regarding the velocity vector's amplitude v and angle θ . In some cases, expressing the momentum components $p_{x(y)}$ in terms of the energy ϵ or even the magnitude of the momentum p is more convenient. Aiming that, in Appendix A, using the Hamiltonian (2) and Eq. (6), we derive an analytical expression [Eq. (A4)] for the energy in analogy to the classic kinetic one. Thus, isolating the velocity of Eq. (A4) and replacing into Eq. (6), the momenta p_x and p_y can be rewritten in terms of the energy, such as

$$p_{x(y)} = \sqrt{\frac{2\epsilon}{M_\theta} \frac{f_{x(y)}(\theta)}{\rho}}, \quad (8)$$

where M_θ corresponds to "the modified total mass of the rotated anisotropic system" [Eq. (A3)]

$$M_\theta \equiv \frac{1}{\rho} \left(\mu_x \cos^2 \theta + \mu_y \sin^2 \theta - \frac{2\mu_x \mu_y}{\mu} \sin \theta \cos \theta \right). \quad (9)$$

To obtain p_x and p_y with respect to the magnitude of the momentum p , we calculate $p^2 = p_x^2 + p_y^2$ by means of Eq. (8), resulting in

$$p^2 = \frac{2\epsilon}{\rho} \left(\mu_x + \mu_y - \frac{\mu_x \mu_y}{M_\theta} \right), \quad (10)$$

which allows us to write the expression

$$p_{x(y)} = g_{x(y)}(\theta) p \cos \theta, \quad (11)$$

whose all the anisotropic aspects of the system are carried out by the $g_{x(y)}(\theta)$ function, given by

$$g_x(\theta) \equiv \frac{f_x(\theta)}{\cos \theta \sqrt{\rho [M_\theta (\mu_x + \mu_y) - \mu_x \mu_y]}}, \quad (12a)$$

$$g_y(\theta) \equiv \frac{f_y(\theta)}{\sin \theta \sqrt{\rho [M_\theta (\mu_x + \mu_y) - \mu_x \mu_y]}}. \quad (12b)$$

According to the equations derived in this section, one can clearly notice that for the isotropic case, i.e., $m_x = m_y = m$ and, consequently, with circular constant energy curve, it would result that $\mu_x = \mu_y$ [Eq. (3)], $1/\mu = 0$ [Eq. (4)], $\rho = 1$, $M_\theta = m$ corresponding to the total mass m of the system [Eq. (A3)], $g_x(\theta) = g_y(\theta) = 1$ [Eqs. (12a) and (12b)], implying, in turn, that the velocity vector would be collinear with the momentum vector [Eq. (11)]. As one shall discuss (Sec. III), the interference and diffraction patterns observed here for the isotropic single- and double-slit cases are analogous to those standard textbooklike patterns, as expected.

B. Tight-binding description

The effective-mass approach presented in the previous Sec. II A can provide a reasonable description of the low-energy dynamics of charge carriers in anisotropic 2D systems within the long-wavelength limit. Nevertheless, a more accurate picture can be obtained from a microscopic model, in which the anisotropy can arise from direction-dependent interaction terms in a tight-binding Hamiltonian [50]. Such an approach has been shown to be suitable for describing electronic, excitonic, and transport properties of various low-dimensional systems based on anisotropic materials [51–66]. In that approach, the Hamiltonian \mathcal{H}_{TB} has the form

$$\mathcal{H}_{\text{TB}} = \sum_i (\epsilon_i + V_i) c_i^\dagger c_i + \sum_{i \neq j} t_{ij} c_i^\dagger c_j, \quad (13)$$

where the sum runs over all sites i and j of the considered lattice. t_{ij} is the hopping parameter between the sites i and j , and c_i (c_i^\dagger) is an operator that annihilates (creates) an electron at site i with onsite energy ϵ_i . To consider the anisotropic aspect of the system, in Sec. II A, direction-dependent masses were assumed within the effective mass approximation. Here, anisotropy is incorporated into the tight-binding model by assuming different values for the hopping parameters along the different crystallographic directions. For a square lattice, it can be easily included by taking $t_{ij} = t_{\bar{x}}$ and $t_{\bar{y}}$ differently along the \bar{x} and \bar{y} directions, respectively. This is illustrated in the insets of Figs. 4(a) and 9(a) for the single- and double-slit anisotropic systems when explored within the tight-binding description. V_i is the onsite potential at site i used here to simulate the rectangular potential barriers to mimic the input screens in the atomistic case. Thus, aiming to address the diffraction problem of single and double slits covering the physical limits from the microscopic to the continuous approaches, next we shall consider comparative discussions and results for these cases within the tight-binding and effective mass frameworks. Numerical calculations within the tight-binding approach were performed using the KWANT Python package [67], which allows the calculation of the probability current density of the single- and double-slit systems and, consequently, the opticlike analogy within the atomistic description for the semiclassical diffraction patterns.

Although our approach is limited to a one-band model case within the long-wavelength and low-energies limits (Sec. II A), consequently, no interband scattering is taken into account, the theoretical framework used here is generic in the sense that similar qualitative features are expected for any system with equivalent effective-mass anisotropy ratio. Therefore, for a multilayer 2D anisotropic system and thus exhibiting a band structure formed by multibands, our model would be equivalent to assuming that one deals separately with each band of each layer such that no modifications on the band curvatures (and, consequently, effective masses) along in-plane directions are considered, regardless the number of layers. A similar assumption was assumed in Refs. [63] and [68] for multilayer phosphorene, in which the effect of stacking phosphorene layers modifies the electron and hole energy levels but not their effective masses. This is based on the fact [63] that the effective masses for multilayer phosphorene systems are shown not to change significantly for $N \geq 5$.

III. RESULTS AND DISCUSSIONS

Next, using the theoretical framework described in Secs. II A and II B, within the effective-mass and tight-binding approaches, respectively, we discuss the effects on the diffraction patterns due to the anisotropy in the single-slit [Fig. 1(a)] and the double-slit systems [Fig. 1(b)], in semiclassical and atomistic perspectives, assuming plane waves incidents on the slits.

A. Single slit

To study the diffraction of electrons in the system schematically represented by Fig. 1(a), we consider that the flat slit has width a and its distance from the screen is sufficiently long such that $D \gg a$, i.e., it means a distance that satisfies Fraunhofer condition [69,70]. In this sense, we can write the wave function Ψ_{sl} reaching the screen at a P point as

$$\begin{aligned} \Psi_{sl}(D, y) &= \int_{-a/2}^{+a/2} C e^{ik_x D} e^{ik_y(y-y')} dy' \\ &= C e^{ik_x D} e^{ik_y y} \frac{2 \sin(k_y a/2)}{k_y}, \end{aligned} \quad (14)$$

where C is the incident wave amplitude, and y is the direction in which the slit is limited in the S -coordinate system. That is, the slit experiment is described here by the S -coordinate system rotated by an angle α of the \bar{S} -coordinate system which, in turn, is aligned with the anisotropic axes of the crystal. The probability density, in turn, is

$$|\Psi_{sl}(D, y)|^2 = C^2 a^2 \frac{\sin^2 \gamma}{\gamma^2}, \quad (15)$$

where $\gamma = k_y a/2$.

Figure 2 shows contour plots of the probability density $|\Psi_{sl}|^2$ [Eq. (15)] as a function of α and θ for three different effective masses ratios m_y/m_x . Figure 2(a) displays the diffraction pattern for the isotropic case ($m_y/m_x = 1$), where, as expected, the probability density is independent of the system rotation angle α and mirror symmetric with respect to the ($\theta = 0$) axis, since the isoenergy is circular and, consequently, the momentum and velocity vectors are now collinear. For different values of effective mass anisotropy, Figs. 2(b) ($m_y/m_x = 2$) and 2(c) ($m_y/m_x = 10$) show that the diffraction patterns are strongly affected by the system orientation concerning the crystallographic axes and the direction of the momentum of the injected beam. Analyzing the maximum amplitude of $|\Psi_{sl}|^2$, one notices an approximately linear relation between the velocity vector's angle θ and the rotation angle α in the range $-\pi/4 < \alpha < \pi/4$. This tendency is not trivial to be immediately identified by just analyzing Eq. (15), although, in this relation, the anisotropic aspect of the system is present just in k_y and, in turn, it depends on both α and θ , as given by any of Eqs. (6), (8), and (11). Note that Eq. (15) is written in a way slightly similar to the ones found in textbooks, except that now $\gamma = k_y a/2$ linearly depends on k_y and which in turn contains all the system's anisotropy as well as information of the orientation of the slits' system setup orientation with respect to the crystallographic axis of the anisotropic 2D material. Moreover, from Figs. 2(b) and 2(c), one has that as the m_y/m_x ratio increases, apart from the

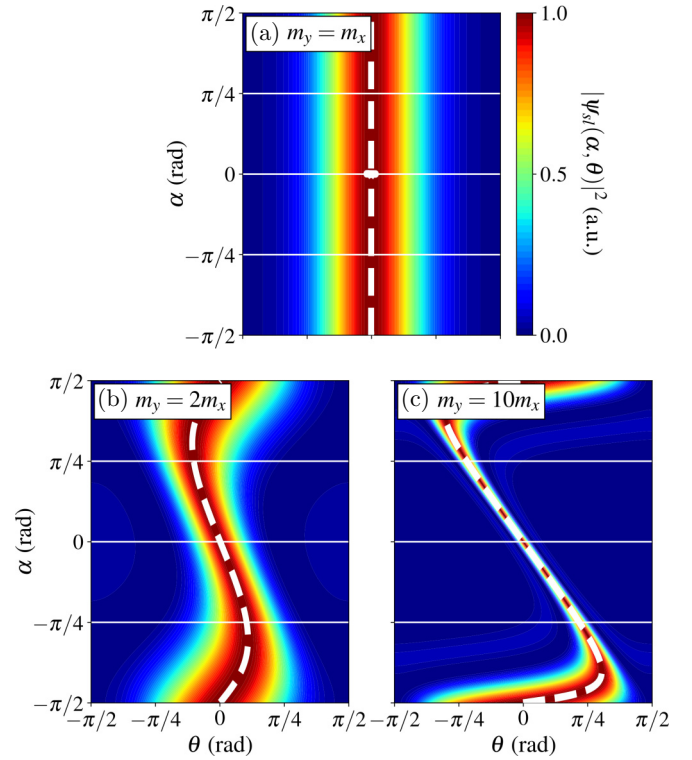


FIG. 2. Contour plot of the probability density $|\Psi_{sl}|^2$ of the single-slit system as a function of the angles α and θ [Eq. (15)] assuming (a) $m_y = m_x$, (b) $m_y = 2m_x$, and (c) $m_y = 10m_x$. We take $\hbar = 1$, $a = 4$, $C = 1$, $\epsilon = 1$, and $m_x = 1$. Solid white lines highlight α values ($-\pi/4$ rad, 0 rad, and $\pi/4$ rad) that will be explored further. Dashed white curves correspond to the analytical expression for the peak position of the central maximum in θ as a function of α given by Eq. (B4).

angular shift, the results for $|\Psi_{sl}|^2$ show a narrowing of the central peak compared with the isotropic case, which can be characterized as a collimation effect. An analytical expression for the peak position of the central maximum in θ as a function of α was derived in Appendix B given by Eq. (B4) and displayed by dashed white curves in Fig. 2.

To emphasize the narrowing of the central peak due to the anisotropy, we show in Fig. 3 the dependence of the probability density $|\Psi_{sl}|^2$ as a function of the angular position θ for fixed values of α , corresponding to the horizontal white lines of Fig. 2 for $\alpha = 0$ rad [Fig. 3(a)], $\alpha = -\pi/4$ rad [Fig. 3(b)], and $\alpha = \pi/4$ rad [Fig. 3(c)]. Results in Fig. 3 for the $m_y = m_x$, $2m_x$, and $10m_x$ cases are denoted by dotted yellow, dashed magenta, and solid blue curves, respectively. In general, note that the curves in Fig. 3 exhibit a $(\sin \gamma / \gamma)^2$ -like behavior, typical of a diffraction pattern for single-slit systems, i.e., with the width and intensity of the single-slit diffraction pattern decreasing as one goes away from the central maximum. The width of the central maximum is determined by the distance between the two first-order minima on either side of the center. The minima of intensity for a $(\sin \gamma / \gamma)^2$ curve occur for $\gamma = \pm\pi, \pm 2\pi, \pm 3\pi, \dots$. Then, the angular width of the central maximum ($2\theta_1$) can be found by taking the angular position of the first minima at $\gamma = \pi$, which results in $\theta_1 = \sin^{-1}(2\pi/k_y a)$, giving $\theta_1 \approx 2\pi/k_y a$

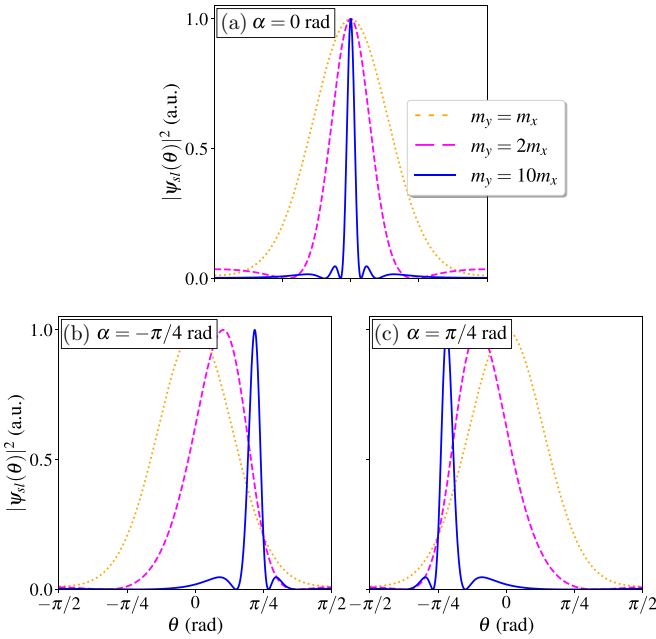


FIG. 3. Diffraction pattern of the single-slit system obtained by the dependence of the probability density $|\Psi_{sl}|^2$ as a function of the angular opening θ of the injected beam [Eq. (15)] taking fixed values of α , namely, (a) $\alpha = 0$ rad, (b) $\alpha = -\pi/4$ rad, and (c) $\alpha = \pi/4$ rad (such values are highlighted in Fig. 2 as solid white lines). Dotted yellow, dashed magenta, and solid blue curves represent, respectively, $m_y = m_x$, $2m_x$, and $10m_x$ cases. We assume the same constant values as in Fig. 2.

in the small-angle approximation or equivalently for wavelengths smaller than the slit width ($\lambda \ll a$). In this way, it becomes clear the independence of the width of the central maximum for the isotropic case (dotted yellow curve) since k_y will be the same regardless of the choice of α . On the other hand, for $m_y \neq m_x$ cases, the anisotropy will induce α and θ dependence on k_y , modifying the angular positions θ_1 of the two first-order minima, the angular distance $2\theta_1$ between them, and consequently the width of the central maxima. It is evident in Fig. 3(a), depicting a narrowing of the central peak the higher the anisotropic of the system, i.e., the angular width $2\theta_1(m_y=10m_x) < 2\theta_1(m_y=2m_x) < 2\theta_1(m_y=m_x)$. From the relation $\theta_1 \approx 2\pi/k_y a$, one has that as the slit width a increases, the width of the central maximum $2\theta_1$ decreases. Therefore, it could lead us to roughly understand the obtained anisotropic-induced narrowing of the central maximum in the single-slit diffraction results, mapping it into the isotropic case as a situation in which we are considering large slit widths, although we are within $D \gg a$ approximation with a negligible slit width. However, the angular shift of the central peak to negative (positive) values of θ for $\alpha = \pi/4$ rad ($\alpha = -\pi/4$ rad) observed in Figs. 3(b) and 3(c) could not be mapped in this isotropic analogy by changing the slit parameters, being a direct consequence of the system's anisotropy.

In addition, by analyzing Fig. 2 beyond the previously discussed linear (α vs θ) region, one can notice that for large α angles and $m_y/m_x \neq 1$ the width of the central maximum $2\theta_1$ increases as it approaches $\alpha = \pm\pi/2$. As seen above, due to the anisotropy of the system, one has

that $k_y \equiv k_y(\theta, \alpha)$, which changes for different system orientations, thus modifying the angular distance $2\theta_1$ of the central maxima of $|\Psi_{sl}|^2$. According to Eqs. (6) and (7b), one can easily obtain for $\alpha = 0$ and $\pi/2$ that $k_y(\alpha = 0) = (v/\hbar)m_y \sin \theta$ and $k_y(\alpha = \pi/2) = (v/\hbar)m_x \sin \theta$, which lead to angular distances in a small-angle approximation given by $2\theta_1(\alpha = 0) \approx [4\pi\hbar/(av \sin \theta)]/m_y$ and $2\theta_1(\alpha = \pi/2) \approx [4\pi\hbar/(av \sin \theta)]/m_x$, respectively. These relations of $2\theta_1$ with $\alpha = 0$ and $\pi/2$ give us a physical insight into the different angular broadening and its mass-ratio inverse tendency for the different system orientations. By taking the ratio between these angular widths, one obtains $\theta_1(\alpha = \pi/2)/\theta_1(\alpha = 0) = m_y/m_x$. From that it is seen, as displayed in Figs. 2 and 3, that as the mass ratio m_y/m_x increases, the difference between the angular widths for $\alpha = 0$ and $\pi/2$ becomes larger (for a fixed mass ratio, compare in Fig. 2 the broadening for $\alpha = 0$ and $\pi/2$).

A variation of the slit alignment (α) results in a pronounced change in the transmission probability of electrons that travel through the slit and are collected at the output lead. Cunha *et al.* [26] theoretically investigated the electronic and transport properties of 2D semiconductor quantum wires with anisotropic effective masses and different orientations with respect to the anisotropic axis. They observed a strong dependence on the spacing of energy levels related to the alignment quantum wire angle and the anisotropy axis showing, for the case of phosphorene and arsenene (two anisotropic 2D semiconductors with the highest effective mass being along opposite directions) that as the quantum wire alignment α increases with respect to the crystallographic axes, the confined energy levels of the system are shifted to lower (upper) values for phosphorene (arsenene), and the spacing between them decreases (increases) too, which in turn increases (decreases) in the number of accessible electronic states. In a quantum-level approach, this result indicates how the transmission probability may be affected due to the variation of the system alignment; for instance, by changing α and consequently increasing (decreasing) the number of accessible electronic states for the propagating modes for a fixed energy range, it leads to an increase (decrease) in the transmission probability.

Next, we investigate the single-slit system from an atomistic perspective using a numerical approach based on the tight-binding model described in Sec. II B. The system consists of a square lattice with a rectangular scattering region (width of $300l$ and length $100l$, where l is the distance between adjacent sites) connected to two semi-infinite leads through which plane waves are injected (lead 0) and collected (lead 1). The single-slit (width of $10l$ and length of $5l$) is simulated using rectangular potential barriers, as shown in Fig. 4(a) highlighted in gold. In this region, the potential used is high enough so that the transmission is negligible. Anisotropy is introduced into the model by assuming different values for the hopping parameter along the \bar{x} and \bar{y} directions, with the hopping parameter defined as $t_{\bar{q}} = -\hbar^2/(m_{\bar{q}}l^2)$ with $q = \{x, y\}$, as illustrated in the inset of Fig. 4(a), and the onsite energy having a value of $-4t_{\bar{x}}$. Then we numerically obtain the probability current density for different values of m_y/m_x and α parameters, chosen to allow a direct comparison with the semiclassical case shown in Figs. 2 and 3, namely, Fig. 4(b) $m_y = m_x$, Figs. 4(c), 4(e), 4(g) $m_y = 2m_x$,

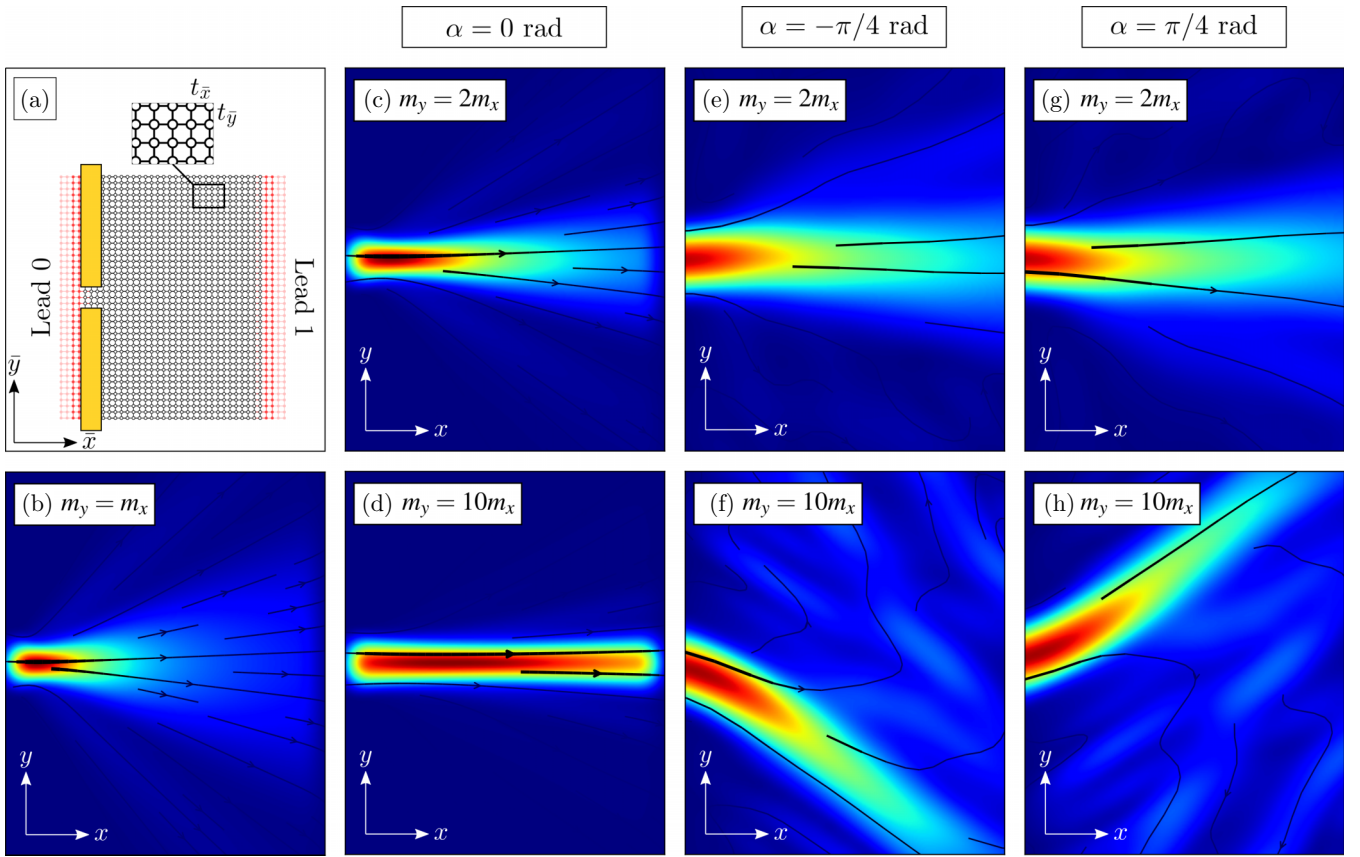


FIG. 4. (a) Schematic illustration of the single-slit system used to numerically simulate the probability current density consisting of a scattering region based on a square lattice with direction-dependent $t_{\bar{x}}$ and $t_{\bar{y}}$ hopping parameters within the tight-binding approximation. In this model, plane waves are injected into the system by lead 0 and collected by lead 1. The highlighted region in gold is subjected to infinite electric potential and acts as a single slit. The system has a width of $300l$ and a length of $100l$, the slit has a width of $10l$ and a length of $5l$, and the electric potential and onsite energy were considered, respectively, $\sim 10^3 \gg t_{\bar{x}}$ and $-4t_{\bar{x}}$. (b)–(h) Represent the probability current densities for the system shown in (a) assuming effective masses such as (b) $m_y = m_x$; (c), (e), (g) $m_y = 2m_x$; and (d), (f), (h) $m_y = 10m_x$, and rotation angle $\alpha = 0$ rad in (c) and (d), $\alpha = -\pi/4$ rad in (e) and (f), and $\alpha = \pi/4$ rad in (g) and (h). We take $\hbar = 1$, $m_x = 1$, $l = 1$, and $\epsilon = 2$.

and Figs. 4(d), 4(f), 4(h) $m_y = 10m_x$, setting $\alpha = 0$ rad in Figs. 4(c) and 4(d), $\alpha = -\pi/4$ rad in Figs. 4(e) and 4(f), and $\alpha = \pi/4$ rad in Figs. 4(g) and 4(h).

The atomistic result for the isotropic case shown in Fig. 4(b) has a direct correspondence with the semiclassical one shown in Fig. 2(a) and in the dotted yellow curve in Fig. 3(a). In this situation, the typical diffraction pattern of a usual semiclassical single-slit system is also obtained, where a wide and intense central maximum and a series of narrower secondary maxima are seen. As previously discussed and shown in Figs. 2 and 3 for the semiclassical case, the main effects on the diffraction pattern due to the anisotropy are (i) a change in the width of the central peak since the probability density becomes concentrated along a particular direction the higher the anisotropy and (ii) a shift of the angular position of the central peak when assumes different orientations of the diaphragm's screen in relation to the anisotropy axes of the material or, equivalently, for different rotation angles of the anisotropy axes concerning the experimental axes. In the atomistic case, the effect (i) is evident when one analyzes Figs. 4(b), 4(c), and 4(d), whereby increasing m_y for fixed m_x it results in the electron beam collimation, as observed by a beam narrowing. Moreover, the effect (ii) is

also verified in the atomistic case by comparing Figs. 4(e) and 4(f) or Figs. 4(g) and 4(h), where one observes upward ($\bar{y} > 0$ axis) and downward ($\bar{y} < 0$ axis) deviations of the electron beam for $\alpha > 0$ and $\alpha < 0$, respectively. This deviation can be understood as follows: for $\alpha = 0$ rad, the S -coordinate system coincides with the \bar{S} coordinate system, i.e., the coordinate system axes are aligned to the system anisotropy axes, so that $\bar{x} = x$ and $\bar{y} = y$, being thus equivalent to analyzing the propagation of the electron beam according to S or \bar{S} . However, for $\alpha \neq 0$, the S - and \bar{S} -coordinate systems are no longer aligned [see the alignment of the elliptical isoenergy curves in Fig. 1(c)], such that the electron beam presents a preferred direction of propagation not aligned with the crystallographic \bar{S} axes, but instead with the direction of lower mass along the x direction, resulting in the central peak maximum deviation according to that direction. Moreover, we emphasize that Figs. 2 and 3 with the semiclassical results of the probability densities for different orientations α and momentum directions θ would represent by analogy the final cross sections of the probability current densities of the atomistic results in the limit when the distance between the input and output leads D in Fig. 4 is sufficiently larger than the slit aperture a , i.e., in the Fraunhofer condition $D \gg a$. In Fig. 4, it was assumed

that $D/a = 30$ and, therefore, a better qualitative agreement between semiclassical and quantum results would be expected the greater this D/a ratio.

Figures 4(b) to 4(h) show a narrowing of the transmitted beam. Such focusing effect shows a dependence on the anisotropy, as seen by comparing the different positions of the focal point in Figs. 4(b) for $m_y = m_x$, 4(c) for $m_y = 2m_x$, and 4(d) for $m_y = 10m_x$ for the $\alpha = 0$ case. In order to understand that dependence of the focal length with respect to the slit aperture and the mass ratio m_y/m_x , we explore in Appendix C, within the quantum-level approach based on the tight-binding model, the interplay between the system anisotropic role and the slit width on the focal length position for the single-slit case. From Fig. 10, as discussed in Appendix C, one notices that the focal length amplitude can be tuned by changing the mass ratio, as seen by comparing the cases of $m_y/m_x = 1$ [Figs. 10(a)–10(e)] and $m_y/m_x = 10$ [Figs. 10(f)–10(j)], exhibiting a large focal length values the larger the mass ratio for $\alpha = 0$ case, and by changing the slit aperture a , presenting the focal point closer to the slit the narrower the slit width.

B. Double slit

1. Interference effect

To calculate interference effects starting with two apertures as in Young's two slits, we consider the double-slit system as illustrated in Fig. 1(b), where the distance between the identical slits is d , their widths are a , and their distances from the screen are sufficiently long such that $D \gg a$. Here, we write Eq. (14) for the wave function for the double-slit system Ψ_{ds}^{in} , which reaches the screen at a point $P = (D, y)$, as a sum of two plane waves, Ψ_{ds1}^{in} and Ψ_{ds2}^{in} , originating, respectively, from the slits S_1 and S_2 , such as

$$\Psi_{ds}^{\text{in}}(D, y) = \Psi_{ds1}^{\text{in}}(D, y) + \Psi_{ds2}^{\text{in}}(D, y), \quad (16a)$$

where

$$\Psi_{ds1}^{\text{in}}(D, y) = A e^{ik_{1x}D} e^{ik_{1y}(y-d/2)}, \quad (16b)$$

$$\Psi_{ds2}^{\text{in}}(D, y) = A e^{ik_{2x}D} e^{ik_{2y}(y+d/2)}, \quad (16c)$$

with (k_{1x}, k_{1y}) and (k_{2x}, k_{2y}) being the incident momentum vectors on the slits S_1 and S_2 . As sketched in Fig. 1(b), the plane waves Ψ_{ds1}^{in} and Ψ_{ds2}^{in} form the angles $\theta_1 = \tan^{-1}(\frac{y-d/2}{D})$ and $\theta_2 = \tan^{-1}(\frac{y+d/2}{D})$ with the \bar{x} axis, respectively. The constant A in Eqs. (16b) and (16c) denotes the incident wave amplitude and y is the direction in which the double slits are limited in the S -coordinate system. From Eqs. (16a), (16b), and (16c) one obtains the probability density given by

$$|\Psi_{ds}^{\text{in}}(D, y)|^2 = 2A^2 \{1 + \cos [(k_{1x} - k_{2x})D + (k_{1y} - k_{2y})y - (k_{1y} + k_{2y})d/2]\}, \quad (17)$$

producing a maximum of interference whenever

$$(k_{1x} - k_{2x})D + (k_{1y} - k_{2y})y - (k_{1y} + k_{2y})d/2 = 2n\pi, \quad (18)$$

and generating a minimum of interference when

$$(k_{1x} - k_{2x})D + (k_{1y} - k_{2y})y - (k_{1y} + k_{2y})d/2 = 2(n + 1/2)\pi, \quad (19)$$

with $n = 0, \pm 1, \pm 2, \dots$

Combining Eqs. (18) and (19) with Eq. (8), for the momenta p_x and p_y with the explicit dependence on the energy, we obtain

$$\begin{aligned} & \left[\frac{f_{1x}(\theta_1)}{\sqrt{M_{\theta_1}}} - \frac{f_{2x}(\theta_2)}{\sqrt{M_{\theta_2}}} \right] D + \left[\frac{f_{1y}(\theta_1)}{\sqrt{M_{\theta_1}}} - \frac{f_{2y}(\theta_2)}{\sqrt{M_{\theta_2}}} \right] y \\ & - \left[\frac{f_{1y}(\theta_1)}{\sqrt{M_{\theta_1}}} + \frac{f_{2y}(\theta_2)}{\sqrt{M_{\theta_2}}} \right] d/2 = \frac{2n\pi \hbar \rho}{\sqrt{2\epsilon}} \end{aligned} \quad (20)$$

for constructive interference and

$$\begin{aligned} & \left[\frac{f_{1x}(\theta_1)}{\sqrt{M_{\theta_1}}} - \frac{f_{2x}(\theta_2)}{\sqrt{M_{\theta_2}}} \right] D + \left[\frac{f_{1y}(\theta_1)}{\sqrt{M_{\theta_1}}} - \frac{f_{2y}(\theta_2)}{\sqrt{M_{\theta_2}}} \right] y \\ & - \left[\frac{f_{1y}(\theta_1)}{\sqrt{M_{\theta_1}}} + \frac{f_{2y}(\theta_2)}{\sqrt{M_{\theta_2}}} \right] d/2 = \frac{2(n + 1/2)\pi \hbar \rho}{\sqrt{2\epsilon}} \end{aligned} \quad (21)$$

for destructive interference, where the de Broglie relation $p_i = \hbar k_i$ was used. These last two expressions [Eqs. (20) and (21)] generalize the conditions for the occurrence of constructive [Eq. (18)] and destructive [Eq. (19)] interferences in the case of an anisotropic system in which the effective mass depends on the direction taken. In Appendix D, we demonstrate that the isotropic case can be obtained analytically as a limiting situation.

Figure 5 displays contour plots of the probability density $|\Psi_{ds}^{\text{in}}|^2$ [Eq. (17)] as a function of angles α and θ for three different effective masses ratios m_y/m_x . For the isotropic case ($m_y/m_x = 1$), Fig. 5(a) shows that the interference pattern presents the typical $\cos^2 \beta$ (with $\beta = \gamma d/a$) behavior of double-slit systems well discussed in the textbooks [33,34], leading to the probability density to be independent of the choice of α and mirror symmetric with respect to the $(\theta = 0)$ axis. As discussed at the end of Sec. II A, for the isotropic case, one has $m_x = m_y$ and consequently $\mu_x = \mu_y$, $g_x(\theta) = g_y(\theta) = 1$, and $p_x = p_y$, thus by taking $k_{1x} = k_{1y} = k_1$ and $k_{2x} = k_{2y} = k_2$ in $|\Psi_{ds}^{\text{in}}|^2$ given by Eq. (17), one finds $|\Psi_{ds}^{\text{in}}(D, y)|^2 \rightarrow 4A^2 \cos^2 \beta$, with $2\beta = (k_1 - k_2)D + (k_1 - k_2)y - (k_1 + k_2)d/2$. β reduces to $\beta = kd/2$ for the case that the two slits radiate in phase ($k_1 = k_2$), and the amplitudes of the waves diffracted by each slit are added up. For different masses ratios, Figs. 5(b) ($m_y/m_x = 2$) and 5(c) ($m_y/m_x = 10$) show that the interference patterns are strongly affected by the choice of α for a given value of θ , i.e., being dependent on the system orientation concerning the anisotropy axes and the orientation of the injected beams. In addition, it is possible to notice from Figs. 5(b) and 5(c) a similar approximately linear tendency in the α range of $-\pi/4 < \alpha < \pi/4$ between the velocity's angle θ and the rotation angle α for the dark and bright interference fringes, presenting a negative linear slope as observed in Figs. 2(b) and 2(c) for the maximum amplitude of $|\Psi_{sl}|^2$ for the anisotropic single-slit system. By comparing Figs. 2(a), 2(b), and 2(c), one notices that the greater the negative slope, the greater the masses ratio m_y/m_x . Moreover, as in the case of the single slit, when

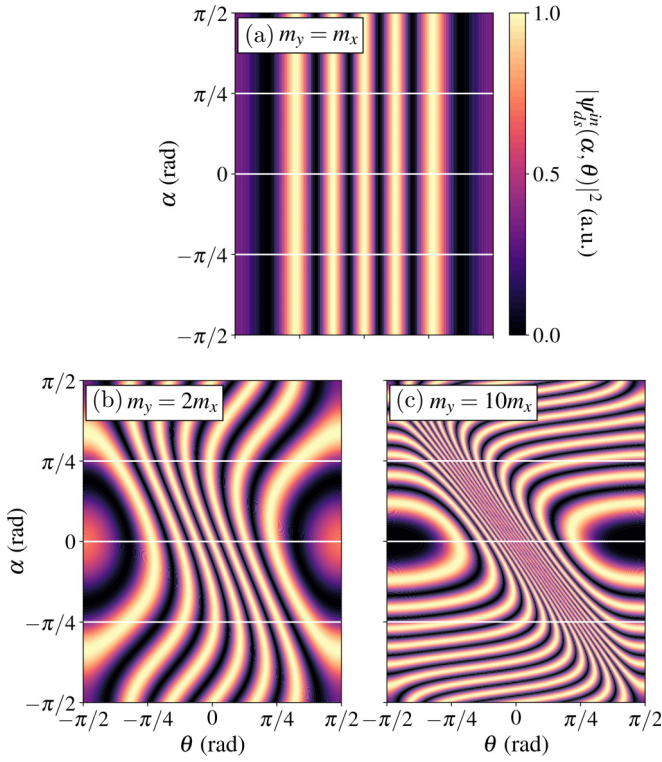


FIG. 5. Contour plot of the probability density $|\Psi_{ds}^{in}|^2$ of the double-slit system as a function of the angles α and θ [Eq. (17)] assuming (a) $m_y = m_x$, (b) $m_y = 2m_x$, and (c) $m_y = 10m_x$. We take $\hbar = 1$, $d = 12$, $A = 1$, $\epsilon = 1$, $m_x = 1$, and $\theta_1 \approx \theta_2 \approx \theta$. Solid white lines highlight α values ($-\pi/4$ rad, 0.0 rad, and $\pi/4$ rad) that will be explored further.

the effective masses ratio m_y/m_x increases, a clear narrowing of the interference peaks for small values of α is observed. Consequently, the amount of light and dark fringes increases as the ratio m_y/m_x increases. This effect is clearly verified in Fig. 6 that shows the dependence of the probability density

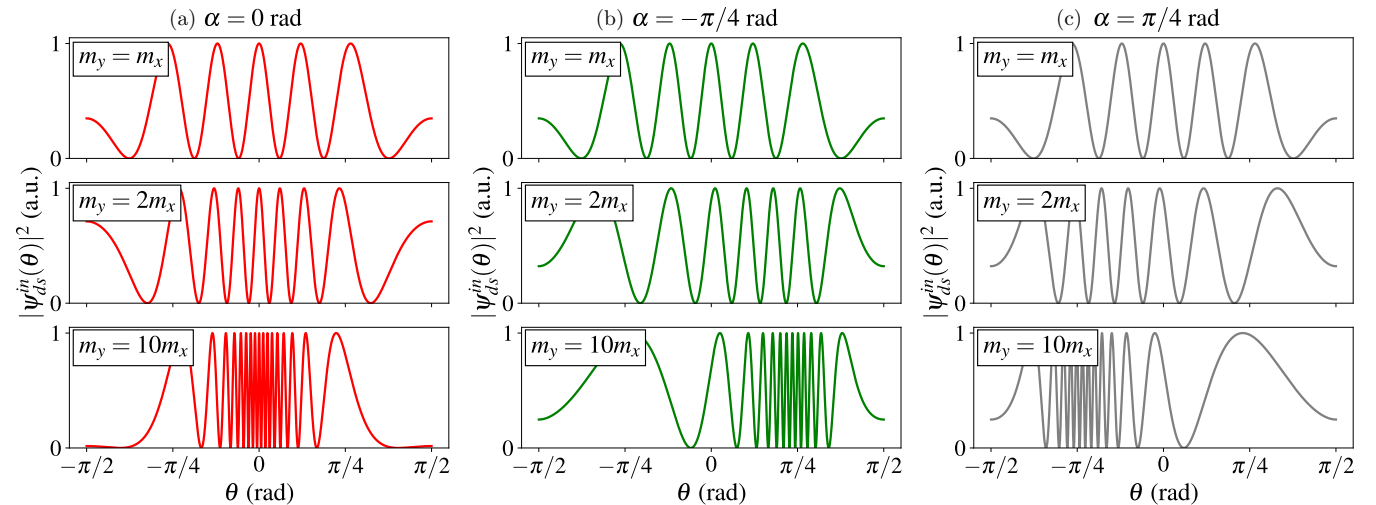


FIG. 6. Interference patterns of the double-slit system obtained by the dependence of the probability density $|\Psi_{ds}^{in}|^2$ as a function of the angular opening θ of the injected beams [Eq. (17)] taking fixed values of α , namely, (a) $\alpha = 0$ rad, (b) $\alpha = -\pi/4$ rad, and (c) $\alpha = \pi/4$ rad (such values are highlighted in Fig. 5 as solid white lines). We assume the same constant values as in Fig. 5.

$|\Psi_{ds}^{in}|^2$ as a function of the angle θ for three fixed values of α , namely, $\alpha = 0$ rad (red curve) in Fig. 6(a), $\alpha = -\pi/4$ rad (green curve) in Fig. 6(b), and $\alpha = \pi/4$ rad (gray curve) in Fig. 6(c), representing them cuts of Fig. 5 for the α values highlighted by the solid white lines. For instance, for $\alpha = 0$ rad in Fig. 6(a) one can see that the increasing of the m_y/m_x ratio leads to a reduction of the wavelength of probability density oscillation, presenting 5, 7, and 17 bright fringes for $m_y/m_x = 1$, $m_y/m_x = 2$, and $m_y/m_x = 10$, respectively. The number of maxima can be extracted from Eq. (18) where the anisotropic aspect of the system is implicitly incorporated in the momentum $k_{1,2|x,y}$ according to Eqs. (6), (8), and (11). Aside from such reduction of the wavelength of probability density oscillation, Figs. 5 and 6 show a focusing of the electron beam around the \bar{x} axis. This is because increasing the ratio m_y/m_x tends to favor the propagation of electrons in the \bar{x} direction. Figure 6(b) [6(c)] for $\alpha = -\pi/4$ rad ($\alpha = \pi/4$ rad) also highlights the shift of the light and dark fringes to positive (negative) values of θ , as already drawn attention to the negative-slope approximately linear behavior in Figs. 5(b) and 5(c).

2. Interference and diffraction

Now, we shall discuss the interference and diffraction effects of the double-slit setup made from anisotropic material. The probability density for the combined effect of interference and diffraction is given by the product of Eqs. (15) and (17) accounting for the diffraction of the single-slit case $|\Psi_{sl}|^2$ and the interference of the double-slit case $|\Psi_{ds}^{in}|^2$, respectively, that is,

$$|\Psi_{ds}^{in,di}|^2 = |\Psi_{sl}|^2 |\Psi_{ds}^{in}|^2, \quad (22)$$

where the superscript $\{in, di\}$ was used to distinguish from the previously analyzed case of sole interference. For the case where both slits radiate in phase, one has that $\theta_1 \approx \theta_2 \approx \theta$ (see

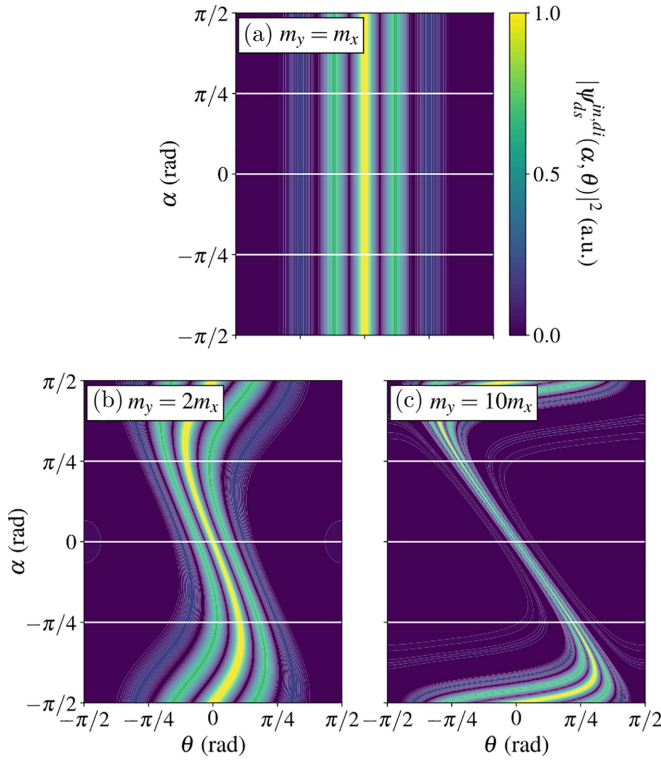


FIG. 7. Contour plot of the probability density $|\Psi_{ds}^{in,di}|^2$ as a function of angles α and θ [Eq. (23)] assuming (a) $m_y = m_x$, (b) $m_y = 2m_x$, and (c) $m_y = 10m_x$. We take $\hbar = 1$, $d = 12$, $A = 1$, $a = 4$, $C = 1$, $\epsilon = 1$, $m_x = 1$, and $\theta_1 \approx \theta_2 \approx \theta$. Solid white lines highlight α values ($-\pi/4$ rad, 0.0 rad, and $\pi/4$ rad) that will be explored further.

Appendix C), and then Eq. (22) becomes

$$|\Psi_{ds}^{in,di}|^2 = I_0 \cos^2 \beta \frac{\sin^2 \gamma}{\gamma^2}, \quad (23)$$

where $I_0 = (2aAC)^2$.

Figure 7 shows contour plots of the probability density $|\Psi_{ds}^{in,di}|^2$, given by Eq. (23), as a function of the angles α and θ for three different masses ratios m_y/m_x . For the isotropic case ($m_y/m_x = 1$) displayed in Fig. 7(a), it is clear to verify the oscillatory behavior of the type proportional to $\cos^2 \beta$ modulated by an envelope function proportional to $\sin^2 \gamma / \gamma^2$ for the probability density. Such behavior is typical of the combined effect of interference and diffraction in an isotropic double-slit system containing light and dark fringes whose amplitudes depend on the value of θ . The interference effect is a consequence of the difference in the path taken by plane waves in the case of the double slits. The diffraction effect, on the other hand, is a result of the deflection of such plane waves as they pass through the individual slits. The pattern projected on the screen contemplates, therefore, both effects. Moreover, Fig. 7(a) shows the symmetric aspect of the probability density oscillation with respect to the ($\theta = 0$) axis for the isotropic case, regardless of the rotation angle α , exhibiting a central peak of greater magnitude at $\theta = 0$ and adjacent peaks with intensities that are reduced for larger angular openings θ . This behavior is well evidenced in the first row of panels in

Fig. 8, which presents horizontal cutting plots of Fig. 7 (solid white lines) for fixed values of α , namely, $\alpha = 0$ in Fig. 8(a), $\alpha = \pi/4$ rad in Fig. 8(b), and $\alpha = -\pi/4$ rad in Fig. 8(c).

When one analyzes the $m_y/m_x \neq 0$ cases, as shown in Figs. 7(b) and 7(c), one can see that for small values of α (approximately in the range $-\pi/4 < \alpha < \pi/4$), the wavelengths associated with the interference pattern and the envelope function decrease as the mass ratio m_y/m_x increases (for m_x fixed). This effect shrinks the peaks, focusing them around a certain θ value. For instance, for $\alpha = 0$ as emphasized in Fig. 8(a) by comparing top, middle, and bottom panels for $m_y/m_x = 1$, $m_y/m_x = 2$, and $m_y/m_x = 10$, respectively, one notices that the injected beam is collimated to ($\theta = 0$) region. Similarly to Fig. 2 for the single-slit system, Fig. 7 exhibits an approximately linear behavior between α and θ for the intensity in the range $-\pi/4 < \alpha < \pi/4$. This is due to the fact that Eq. (23) has the $|\Psi_{sl}|^2$ contribution that modulates the probability density of the double-slit system similarly as displayed in Fig. 2 for the single-slit system. Furthermore, in analogy to Fig. 2 for single slit, one also observes in Fig. 7 for an anisotropic double-slit system a shift of the center of the oscillation. This angular displacement of the central maximum in the probability density is a consequence of the anisotropic nature of the investigated systems and is evident in Figs. 8(b) and 8(c), where the peaks are shifted for positive (negative) values of θ when analyses fixed α with negative (positive) value.

From the atomistic perspective, we numerically simulate the double-slit system shown in Fig. 1(b) similarly to that employed in the single-slit case discussed in Sec. III A. Figure 9(a) schematically illustrates the simulated double-slit quantum system, theoretically described here by the tight-binding model with direction-dependent hopping parameters (Sec. II B), in which it was assumed a square lattice with rectangular potential barriers with two narrow channels close to lead 0 to model the two slits. The onsite energy in Eq. (13) is non-null for the atomic sites in the gold region in Fig. 9(a). The slits are $10l$ wide and $5l$ long and are separated by a distance $d = 5l$. The scattering region is $300l$ wide and $100l$ long. The probability current density is obtained numerically for different configurations of the mass ratio m_y/m_x and α values, namely, Fig. 9(b) $m_y/m_x = 1$; Figs. 9(c), 9(e), 9(g) $m_y/m_x = 2$; and Figs. 9(d), 9(f), 9(h) $m_y/m_x = 10$; setting $\alpha = 0$ rad in Figs. 9(c) and 9(d), $\alpha = -\pi/4$ rad in Figs. 9(e) and 9(f), and $\alpha = \pi/4$ rad in Figs. 9(g) and 9(h) in order to compare with the results in Figs. 7 and 8. The isotropic case shown in Fig. 9(b) has a direct correspondence with the semiclassical results displayed in Fig. 7(a) and with the upper row of panels in Fig. 8, in which the typical pattern of a usual double-slit isotropic system is observed, i.e., a central maximum and adjacent peaks with decreasing amplitudes. The effect of reducing the wavelength for regions close to $\alpha = 0$ rad, discussed previously for the semiclassical case in Fig. 8(a), can be verified by comparing Figs. 9(b), 9(c), and 9(d). Note that by increasing the masses ratio, one results in the convergence of the electron beam around the \bar{x} axis. The discrepancy between the semiclassical and quantum results is due to the size of the scattering region in the latter case, as can be seen by the probability current density lines that reach lead 1 in Fig. 9(d), which presents a behavior which is

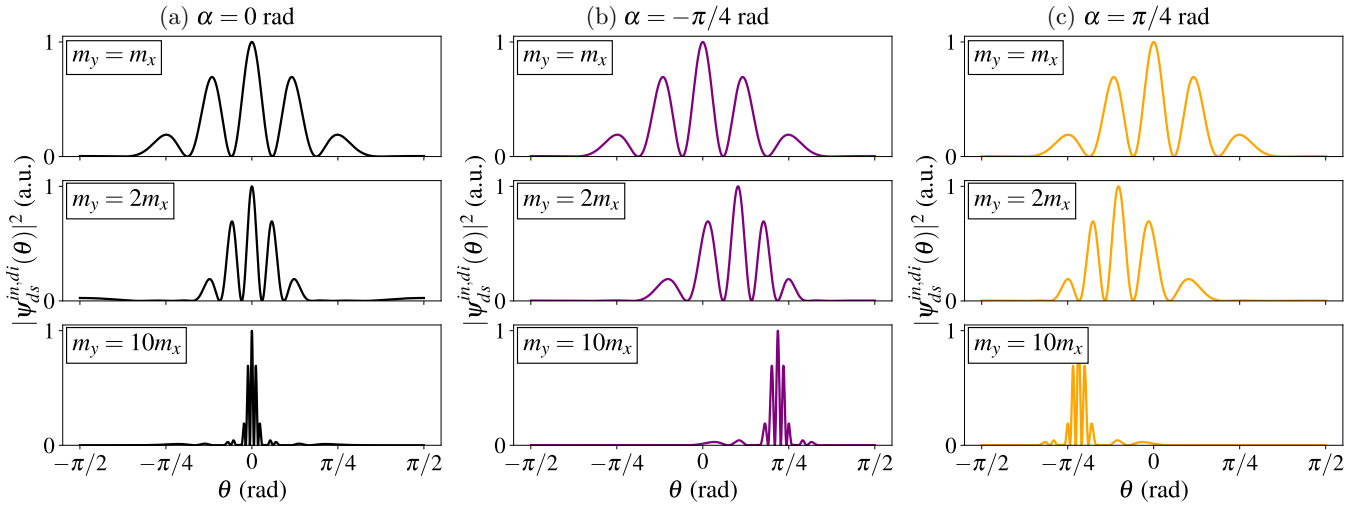


FIG. 8. Diffraction and interference patterns of the double-slit system obtained by the dependence of the probability density $|\Psi_{ds}^{in,di}|^2$ as a function of the angular opening θ of the injected beams [Eq. (23)] taking fixed values of α , namely, (a) $\alpha = 0$ rad, (b) $\alpha = -\pi/4$ rad, and (c) $\alpha = \pi/4$ rad (such values are highlighted in Fig. 7 as solid white lines). We assume the same constant values as in Fig. 7 and take $\theta_1 \approx \theta_2 \approx \theta$.

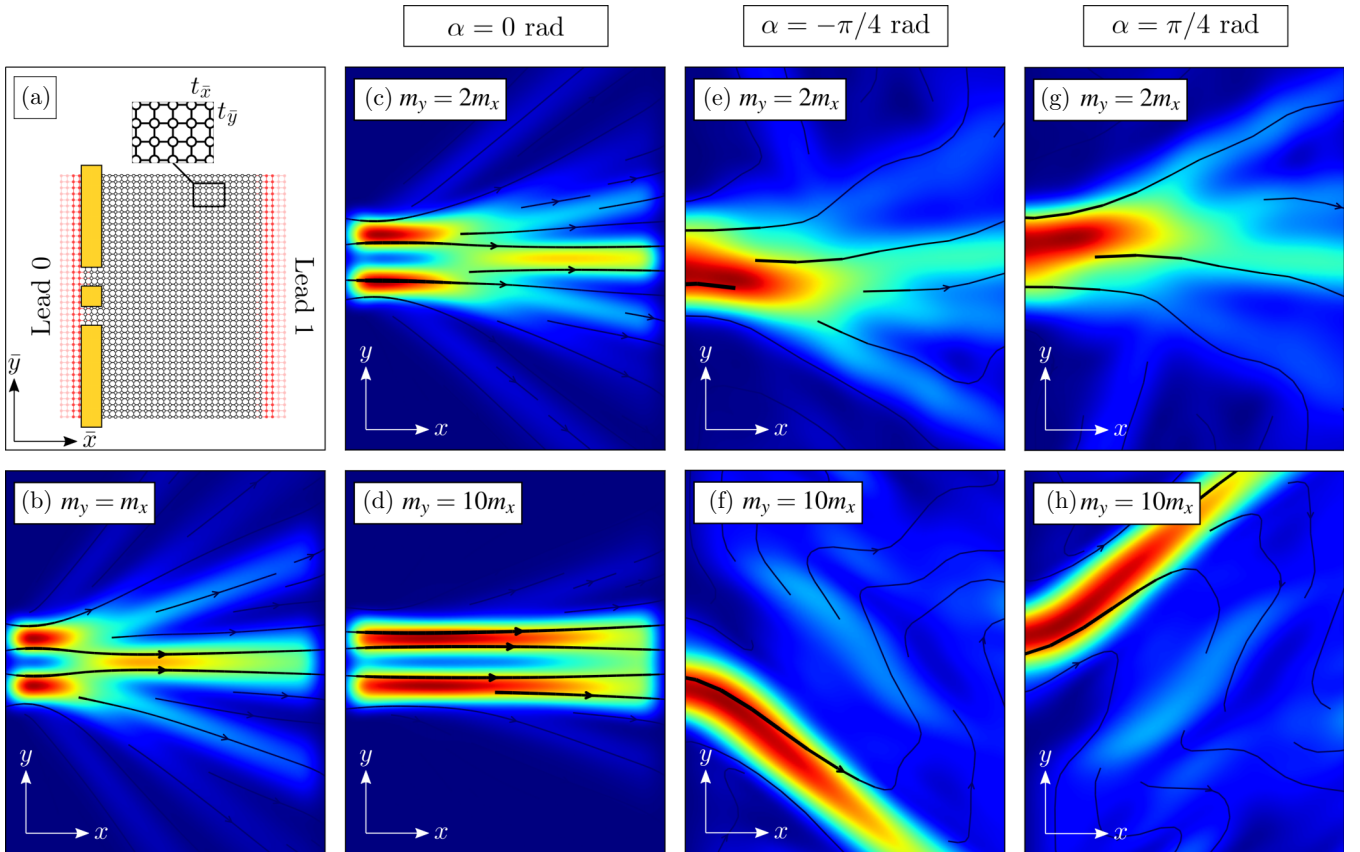


FIG. 9. (a) Schematic illustration of the double-slit system used to numerically simulate the probability current density consisting of a scattering region based on a square lattice with direction-dependent t_x and t_y hopping parameters within the tight-binding approximation. Leads 0 and 1 correspond to the injected and collected leads, respectively. The highlighted region in gold is subjected to infinite electric potential and acts as a double slit. The system has a width of $300l$ and a length of $100l$, the slits are $10l$ wide and $5l$ long, the distance between the slits is $d = 5l$, and the electric potential and onsite energy were considered, respectively, $\sim 10^3 \gg t_x$ and $-4t_x$. (b)–(h) Represent the probability current densities for the system shown in (a) assuming (b) $m_y = m_x$, (c), (e), (g) $m_y = 2m_x$, and (d), (f), (h) $m_y = 10m_x$, and rotation angle $\alpha = 0$ rad in (c), (d), $\alpha = -\pi/4$ rad in (e), (f), and $\alpha = \pi/4$ rad in (g), (h). We take $\hbar = 1$, $m_x = 1$, $l = 1$, and $\epsilon = 2$.

still converging and will therefore present a narrowing of the injected beam, as expected in the semiclassical case shown in Fig. 8(a). The beam deflections in Figs. 9(e) and 9(g) are due to the system finite size along the y direction used here to simulate the double-slit experiment and owing to a not sufficiently long distance D between the input and output leads, such that reflections with the simulation box boundaries are clearly interfering the central peak of the probability current densities. However, in general, the tight-binding (Fig. 9) and semiclassical (Fig. 8) results agree well qualitatively, as discussed for the single slit in Sec. III A and in the present section III B for the double-slit case. In addition, the effect of shifting the central maximum is verified by comparing Figs. 9(e) and 9(f) or Figs. 9(g) and 9(h), where one observes a deviation of the electron beam in an analogous way to the semiclassical case previously investigated. Therefore, the quantum simulations and the semiclassical results show excellent agreement on the main features of the anisotropic role in the single- and double-slit systems.

IV. CONCLUSION

The diffraction of electrons through single and double slits was examined, considering that the medium through which electrons propagate is anisotropic. The influence on the diffraction patterns due to different orientations of the diaphragm's screen, with the single and double slits, with respect to the anisotropic axis of the system was also explored. In addition to the diffraction analysis, interference effects and the conditions for constructive and destructive interferences were studied for the double-slit case. For that, two different frameworks were employed: (i) a semiclassical approach within the effective-mass approximation, where the anisotropy was incorporated into the system by assuming direction-dependent effective masses, and (ii) an atomistic-level approach based on the tight-binding formalism, where the anisotropy was included by taking direction-dependent hopping energies. In both cases, it was assumed the Fraunhofer diffraction criteria, in which the characteristic length of the slit a is much smaller than its distance from the detection screen D , i.e., the case of the diffraction at infinity with $a \ll D$. Analyzing the intensity of the diffracted wave, we showed that (i) both models qualitatively predicted similar results; the anisotropy effect on the diffraction pattern in a 2D system involves two general effects: (ii) modulation in the wavelength and (iii) apparent deviation of the diffracted electron beam with respect to the system orientation and its alignment to the anisotropic axis. Finally, we hope that our optical analog results will prove helpful for designing anisotropic semiconductor-based quantum devices owing to the possibility of controlling the direction of the carriers' trajectories.

ACKNOWLEDGMENTS

This work was supported by the Brazilian Council for Research (CNPq), through the PRONEX/FUNCAP, Universal, and PQ programs, the Brazilian National Council for the Improvement of Higher Education (CAPES). D.R.C gratefully acknowledges the support from CNPq Grants No.

313211/2021-3, No. 437067/2018-1, No. 423423/2021-5, No. 408144/2022-0 and the Research Foundation–Flanders (FWO).

APPENDIX A: OBTAINING VELOCITY AS A FUNCTION OF EFFECTIVE MASSES AND ENERGY

Here, we obtain an analytical expression for the system energy in analogy to the classical kinetic one, e.g., $\epsilon = M_\theta v^2/2$, i.e., in terms of an explicit dependence on the velocity amplitude v . In contrast to the semiclassical case, one has a new definition for the total mass term $M_\theta \equiv M_\theta(\theta, \alpha, m_x, m_y)$ that shall incorporate the anisotropic features of the system. Aiming that using the p_x and p_y components of momentum \mathbf{p} of Eq. (6), one has that

$$p_x^2 = \frac{v^2}{\rho^2} \left[(\mu_x \cos \theta)^2 + \left(\frac{\mu_x \mu_y}{\mu} \sin \theta \right)^2 - 2 \frac{\mu_x^2 \mu_y}{\mu} \sin \theta \cos \theta \right], \quad (\text{A1a})$$

$$p_y^2 = \frac{v^2}{\rho^2} \left[(\mu_y \sin \theta)^2 + \left(\frac{\mu_x \mu_y}{\mu} \cos \theta \right)^2 - 2 \frac{\mu_x \mu_y^2}{\mu} \sin \theta \cos \theta \right], \quad (\text{A1b})$$

$$p_x p_y = \frac{v^2}{\rho^2} \left[\mu_x \mu_y \sin \theta \cos \theta - \frac{\mu_x^2 \mu_y}{\mu} \cos^2 \theta - \frac{\mu_x \mu_y^2}{\mu} \sin^2 \theta + \left(\frac{\mu_x \mu_y}{\mu} \right)^2 \sin \theta \cos \theta \right]. \quad (\text{A1c})$$

Replacing them into the Hamiltonian (2) and taking the associated system energy, one obtains

$$\epsilon = \frac{1}{2} M_\theta v^2, \quad (\text{A2})$$

where

$$M_\theta \equiv \frac{1}{\rho} \left(\mu_x \cos^2 \theta + \mu_y \sin^2 \theta - \frac{2\mu_x \mu_y}{\mu} \sin \theta \cos \theta \right), \quad (\text{A3})$$

with $\rho = 1 - \mu_x \mu_y / \mu^2$. Isolating v in Eq. (A2), one gets

$$v = \sqrt{\frac{2\epsilon}{M_\theta}}. \quad (\text{A4})$$

APPENDIX B: ANALYTICAL EXPRESSION FOR THE MAXIMUM OF THE CENTRAL PEAK FOR THE ANISOTROPIC SINGLE-SLIT SETUP

An analytical expression describing the peak position of the central maximum in θ as a function of α can be derived by Taylor expanding Eq. (15) and then calculating the gradient vector of $|\Psi_{sl}|^2$ and equating it to zero, i.e.,

$$\nabla_{\theta\alpha} |\Psi_{sl}|^2 = \left(\frac{\partial |\Psi_{sl}|^2}{\partial k_y} \frac{dk_y}{d\theta}, \frac{\partial |\Psi_{sl}|^2}{\partial k_y} \frac{dk_y}{d\alpha} \right) = (0, 0). \quad (\text{B1})$$

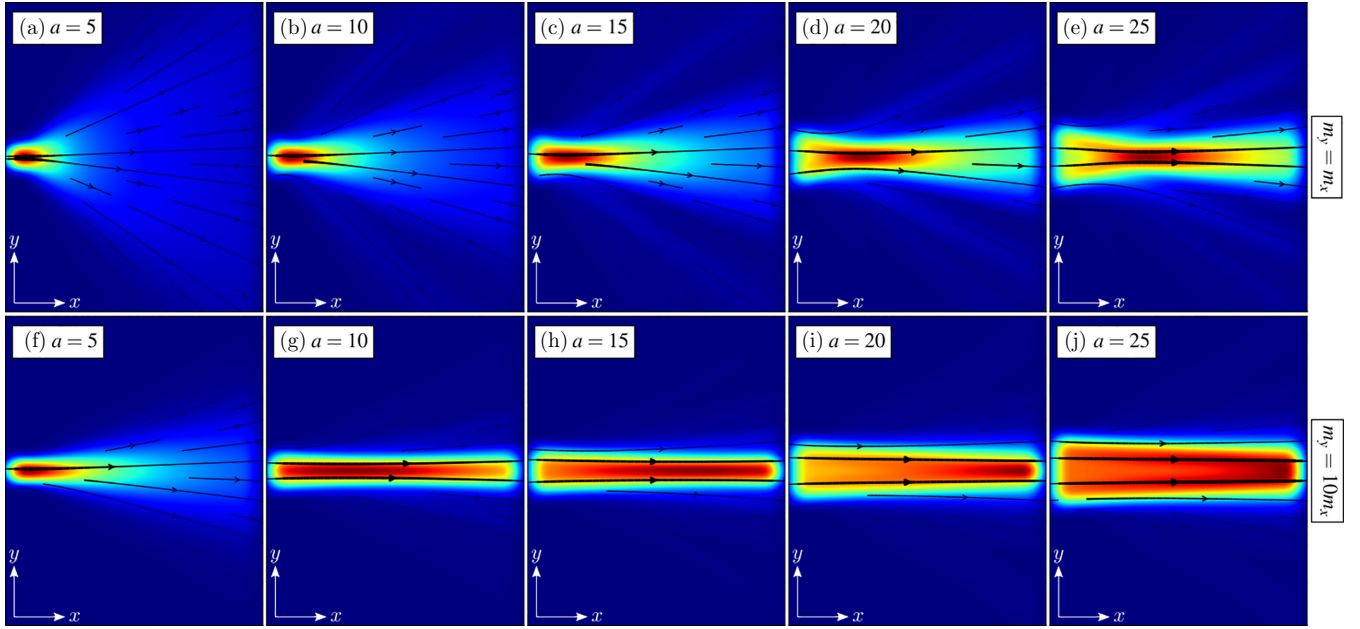


FIG. 10. Probability current densities obtained via the tight-binding model assuming effective masses (a)–(e) $m_y = m_x$ and (f)–(j) $m_y = 10m_x$, and taking different slit widths: (a), (f) $a = 5$, (b), (g) $a = 10$, (c), (h) $a = 15$, (d), (i) $a = 20$, and (e), (j) $a = 25$. We take the same system parameters as in Fig. 2.

Taking up to the second order on k_y in Eq. (15), one obtains

$$|\Psi_{sl}(D, y)|^2 \approx C^2 a^2 \left(1 - \frac{a^2 k_y^2}{12} \right), \quad (\text{B2})$$

with $k_y \equiv k_y(\theta, \alpha)$. Replacing Eq. (B2) into (B1), it results in

$$\frac{d|\Psi_{sl}|^2}{d\theta} = -\frac{c^2 a^4 v^2}{24 \hbar^2} [(m_x + m_y) \cos \theta - (m_x - m_y) \cos(2\alpha + \theta)][(m_x + m_y) \sin \theta - (m_x - m_y) \sin(2\alpha + \theta)], \quad (\text{B3a})$$

$$\frac{d|\Psi_{sl}|^2}{d\alpha} = \frac{c^2 a^4 v^2}{12 \hbar^2} (m_x - m_y) \cos(2\alpha + \theta) [(m_x + m_y) \sin \theta - (m_x - m_y) \sin(2\alpha + \theta)]. \quad (\text{B3b})$$

Isolating θ as a function of α , one finds

$$\theta_m(\alpha) = 2 \arctan \left\{ \frac{-m_x \sin^2 \alpha - m_y \cos^2 \alpha + \sqrt{m_x^2 \sin^2 \alpha + m_y^2 \cos^2 \alpha}}{(m_x - m_y) \sin \alpha \cos \alpha} \right\}. \quad (\text{B4})$$

A local maximum point can be found by calculating the Hessian matrix and performing the second derivative test, such that if the Hessian is negative-definite at the critical point, then the function attains an isolated local maximum at the critical point. However, our goal was to derive an expression that described the tendency of the central maximum for the single-slit case, as given by Eq. (B4) and showed by the dashed white curves in Figs. 2(b) and 2(c).

APPENDIX C: FOCAL LENGTH

To demonstrate the focusing effect of the waves transmitted through the single slit on the probability current density,

its connection with slit aperture size, and the role of the anisotropy in the focal length measured from the slit, we show in Fig. 10 numerical results obtained by using the tight-binding framework described in Sec. II B for isotropic and anisotropic single-slit systems taking different slit widths. The quantum mechanics' calculated results in Figs. 10(a)–10(j) show that the focus point (around the dark red color region in the contour plots) is pushed further from the slit the wider the slit, regardless of whether the system is isotropic or anisotropic, as depicted in Figs. 10(a)–10(e) for $m_y = m_x$ and in Figs. 10(f)–10(j) for $m_y = 10m_x$. Moreover, by comparing the results for a fixed slit width as shown in Figs. 10(a) and 10(f) for $a = 5$, 10(b) and 10(g) for $a = 10$, 10(c) and 10(h) for $a = 15$, 10(d) and 10(i) for $a = 20$, and 10(e) and 10(j)

for $a = 25$, one can observe that the focal length is larger the larger the mass ratio m_y/m_x .

Furthermore, as discussed in Sec. III A, the angular width $2\theta_1$ of the first peak of the probability density, i.e., the angle at which a first minimum is obtained, being equivalent to considering the prerequisite for dark fringes that must induce destructive interference, resulting to a path difference λ , is connected with the slit width a by the relation $a \sin \theta_1 = \lambda = 2\pi/k_y$. For small-angles regime, one has $\sin \theta_1 \approx \theta_1 = \lambda/a = 2\pi/(ak_y)$. From that, one can note that the angular width of the fringes in the diffraction pattern collected in the screen in a single-slit experiment is inversely proportional to the slit width a , meaning that narrower (wider) slits a produce wider (narrower) fringes. The reason for that is linked to the fact that a narrower slit acts as a source of diffraction that allows it to pass waves over a wider range of angles, such that these more widely diverging waves then interfere to form wider-spaced fringes at the collecting screen. Although the aforementioned discussions are valid for a Fraunhofer single-slit setup, describing semiclassical diffraction patterns, one can qualitatively relate them to the opticlke analogy of atomistic results shown in Fig. 10, which demonstrates such wider-spaced behavior on the probability current densities the narrower the slit width.

APPENDIX D: OBTAINING THE ISOTROPIC CASE AS A LIMIT SITUATION IN THE CASE OF DOUBLE SLIT

Taking $\theta_1 \approx \theta_2 \approx \theta$ in Eqs. (20) and (21), it is easy to see that in this approximation, the first two terms of these expressions approach zero. Using the even characteristic of the cosine function present in Eq. (17), we can write Eqs. (20)

and (21) by omitting the negative sign of the third term so that

$$f_y(\theta)d = Nh\sqrt{\frac{\rho}{2\epsilon}}, \quad (D1)$$

where $N = n$ generates constructive interference and $N = n + \frac{1}{2}$ generates destructive interference. Explicitly, we have

$$\frac{\mu_y \sin \theta - \frac{\mu_x \mu_y}{\mu} \cos \theta}{\sqrt{M_\theta \rho}} d = Nh\sqrt{\frac{\rho}{2\epsilon}}. \quad (D2)$$

Considering the isotropic limiting case, that is, $\mu_x = \mu_y = m_x = m_y = m$ and $\mu^{-1} = 0$, we obtain $\rho = 1$ and $M_\theta = m$, resulting in the following usual expression:

$$d \sin \theta = N \frac{h}{\sqrt{2m\epsilon}} = N\lambda. \quad (D3)$$

On the other hand, for the anisotropic case ($m_x \neq m_y$) but also taking $\mu^{-1} = 0$, we have

$$\frac{\mu_y \sin \theta}{\sqrt{\mu_x \cos^2 \theta + \mu_y \sin^2 \theta}} d = N \frac{h}{\sqrt{2\epsilon}}, \quad (D4)$$

which can be rewritten as

$$\sin \theta = \frac{N \left(\frac{h}{d\sqrt{2\epsilon}} \right) \sqrt{\mu_x}}{\sqrt{\mu_y^2 - N^2 \left(\frac{h}{d\sqrt{2\epsilon}} \right)^2 (\mu_y - \mu_x)}}, \quad (D5)$$

and leads to Eq. (D3) for $\mu_x = \mu_y = m$ as expected. The approximation $\mu^{-1} \rightarrow 0$ can be obtained from the following situations: (i) when the anisotropy is weak, that is, $m_x \approx m_y$, so that we can approximate $\mu^{-1} \rightarrow 0$ due to Eq. (4), or (ii) when regardless of the anisotropy, we are taking rotations with small angles, where we can make $\sin \theta \approx \theta$ and $\cos \theta \approx 1$, resulting again in $\mu^{-1} \rightarrow 0$ by Eq. (4).

-
- [1] S. Datta, *Quantum Transport: Atom to Transistor* (Cambridge University Press, Cambridge, 2005).
- [2] S. Datta, *Electronic Transport in Mesoscopic Systems* (Cambridge University Press, Cambridge, 1997).
- [3] K. S. Novoselov, A. K. Geim, S. V. Morozov, D. Jiang, Y. Zhang, S. V. Dubonos, I. V. Grigorieva, and A. A. Firsov, *Science* **306**, 666 (2004).
- [4] A. K. Geim, *Science* **324**, 1530 (2009).
- [5] K. S. Novoselov, V. I. Fal'ko, L. Colombo, P. R. Gellert, M. G. Schwab, and K. Kim, *Nature (London)* **490**, 192 (2012).
- [6] A. K. Geim and K. S. Novoselov, *Nat. Mater.* **6**, 183 (2007).
- [7] A. H. Castro Neto, F. Guinea, N. M. R. Peres, K. S. Novoselov, and A. K. Geim, *Rev. Mod. Phys.* **81**, 109 (2009).
- [8] A. Molle, C. Grazianetti, L. Tao, D. Taneja, M. H. Alam, and D. Akinwande, *Chem. Soc. Rev.* **47**, 6370 (2018).
- [9] A. Kara, H. Enriquez, A. P. Seitsonen, L. C. L. Y. Voon, S. Vizzini, B. Aufray, and H. Oughaddou, *Surf. Sci. Rep.* **67**, 1 (2012).
- [10] V. V. Cheianov, V. Fal'ko, and B. L. Altshuler, *Science* **315**, 1252 (2007).
- [11] L. Banszerus, M. Schmitz, S. Engels, M. Goldsche, K. Watanabe, T. Taniguchi, B. Beschoten, and C. Stampfer, *Nano Lett.* **16**, 1387 (2016).
- [12] K. Wang, M. M. Elahi, L. Wang, K. M. Habib, T. Taniguchi, K. Watanabe, J. Hone, A. W. Ghosh, G.-H. Lee, and P. Kim, *Proc. Natl. Acad. Sci. USA* **116**, 6575 (2019).
- [13] U. Sivan, M. Heiblum, C. P. Umbach, and H. Shtrikman, *Phys. Rev. B* **41**, 7937 (1990).
- [14] R. R. Hartmann, N. J. Robinson, and M. E. Portnoi, *Phys. Rev. B* **81**, 245431 (2010).
- [15] J. R. Williams, T. Low, M. S. Lundstrom, and C. M. Marcus, *Nat. Nanotechnol.* **6**, 222 (2011).
- [16] A. Carvalho, M. Wang, X. Zhu, A. S. Rodin, H. Su, and A. H. Castro Neto, *Nat. Rev. Mater.* **1**, 16061 (2016).
- [17] C. Kamal and M. Ezawa, *Phys. Rev. B* **91**, 085423 (2015).
- [18] S. Manzeli, D. Ovchinnikov, D. Pasquier, O. V. Yazyev, and A. Kis, *Nat. Rev. Mater.* **2**, 17033 (2017).
- [19] C. Gong, Y. Zhang, W. Chen, J. Chu, T. Lei, J. Pu, L. Dai, C. Wu, Y. Cheng, T. Zhai *et al.*, *Adv. Sci.* **4**, 1700231 (2017).
- [20] H.-X. Zhong, S. Gao, J.-J. Shi, and L. Yang, *Phys. Rev. B* **92**, 115438 (2015).
- [21] M. Rahman, K. Davey, and S.-Z. Qiao, *Adv. Funct. Mater.* **27**, 1606129 (2017).
- [22] J. Dai and X. C. Zeng, *Angew. Chem. Int. Ed.* **54**, 7572 (2015).
- [23] H. Yang, H. Jussila, A. Autere, H.-P. Komsa, G. Ye, X. Chen, T. Hasan, and Z. Sun, *ACS Photonics* **4**, 3023 (2017).

- [24] X. Li, C. Chen, Y. Yang, Z. Lei, and H. Xu, *Adv. Sci.* **7**, 2002320 (2020).
- [25] S. M. Cunha, D. R. da Costa, G. O. de Sousa, A. Chaves, J. M. Pereira, Jr., and G. A. Farias, *Phys. Rev. B* **99**, 235424 (2019).
- [26] S. M. Cunha, D. R. da Costa, L. C. Felix, A. Chaves, and J. M. Pereira, Jr., *Phys. Rev. B* **102**, 045427 (2020).
- [27] Y. Betancur-Ocampo, F. Leyvraz, and T. Stegmann, *Nano Lett.* **19**, 7760 (2019).
- [28] Y. Betancur-Ocampo, E. Paredes-Rocha, and T. Stegmann, *J. Appl. Phys.* **128**, 114303 (2020).
- [29] S. Dana, M. Zare, and P. Zamani, *Phys. E (Amsterdam)* **124**, 114239 (2020).
- [30] F. R. V. Araújo, D. R. da Costa, A. C. S. Nascimento, and J. M. Pereira, Jr., *J. Phys.: Condens. Matter* **32**, 425501 (2020).
- [31] H. M. Abdullah, D. R. da Costa, H. Bahlouli, A. Chaves, F. M. Peeters, and B. Van Duppen, *Phys. Rev. B* **100**, 045137 (2019).
- [32] F. R. V. Araújo, R. N. S. Magalhães, I. V. de Sousa, Jr., A. C. S. Nascimento, and D. R. da Costa, *Rev. Bras. Ensino Fis.* **44**, e20220132 (2022).
- [33] R. P. Feynman, R. B. Leighton, and M. Sands, *The Feynman Lectures on Physics*, Vol. III (Basic Books, New York, 2011), pp. 1–11.
- [34] J. W. Jewett, Jr. and R. A. Serway, *Física para Cientistas e Engenheiros*, Vol. 4 (Cengage Learning, Boston, 2012), pp. 74–97.
- [35] C. Brand, S. Troyer, C. Knobloch, O. Cheshnovsky, and M. Arndt, *Am. J. Phys.* **89**, 1132 (2021).
- [36] J. Sánchez-Ruiz, *Phys. Rev. A* **57**, 1519 (1998).
- [37] W. Xiang-Yao, Z. Bai-Jun, L. Hai-Bo, L. Jing-Bin, L. Xiao-Jing, W. Li, Z. Chun-Li, L. Bing, F. Xi-Hui, and G. Yi-Qing, *Chin. Phys. Lett.* **24**, 2741 (2007).
- [38] R. Tirole, S. Vezzoli, E. Galiffi, I. Robertson, D. Maurice, B. Tilmann, S. A. Maier, J. B. Pendry, and R. Sapienza, *Nat. Phys.* **19**, 999 (2023).
- [39] D. Shapiro and W. C. Henneberger, *J. Phys. A: Math. Gen.* **22**, 3605 (1989).
- [40] R. Bach, D. Pope, S.-H. Liou, and H. Batelaan, *New J. Phys.* **15**, 033018 (2013).
- [41] P. Yeh, *Surf. Sci.* **96**, 41 (1980).
- [42] F. Liu and J. Li, *Phys. Rev. Lett.* **114**, 103902 (2015).
- [43] F. V. Ignatovich and V. K. Ignatovich, *Phys. Usp.* **55**, 709 (2012).
- [44] R. Dixon, *IEEE J. Quantum Electron.* **3**, 85 (1967).
- [45] Y. A. Kravtsov, O. N. Naida, and A. A. Fuki, *Phys. Usp.* **39**, 129 (1996).
- [46] S. P. Palto, *J. Exp. Theor. Phys.* **92**, 552 (2001).
- [47] M. G. Cohen, *J. Appl. Phys.* **38**, 3821 (1967).
- [48] V. S. Zapasskii and G. G. Kozlov, *Phys. Usp.* **42**, 817 (1999).
- [49] J. Elser and V. A. Podolskiy, *Phys. Rev. Lett.* **100**, 066402 (2008).
- [50] W. P. Lima, F. R. V. Araújo, D. R. da Costa, S. H. R. Sena, and J. M. Pereira, Jr., *Braz. J. Phys.* **52**, 42 (2022).
- [51] C. J. Páez, K. DeLello, D. Le, A. L. C. Pereira, and E. R. Mucciolo, *Phys. Rev. B* **94**, 165419 (2016).
- [52] I. Schnell, M. D. Jones, S. P. Rudin, and R. C. Albers, *Phys. Rev. B* **74**, 054104 (2006).
- [53] D. A. Prishchenko, V. G. Mazurenko, M. I. Katsnelson, and A. N. Rudenko, *2D Mater.* **4**, 025064 (2017).
- [54] K. H. Ahn and A. J. Millis, *Phys. Rev. B* **61**, 13545 (2000).
- [55] D. Li, C. Barreateau, M. R. Castell, F. Silly, and A. Smogunov, *Phys. Rev. B* **90**, 205409 (2014).
- [56] I. I. Mazin, D. A. Papaconstantopoulos, and D. J. Singh, *Phys. Rev. B* **61**, 5223 (2000).
- [57] Q. Li, C. M. Soukoulis, E. N. Economou, and G. S. Grest, *Phys. Rev. B* **40**, 2825 (1989).
- [58] V. Sorkin and Y. W. Zhang, *Nanotechnology* **27**, 395701 (2016).
- [59] D. Li, A. Smogunov, C. Barreateau, F. Ducastelle, and D. Spanjaard, *Phys. Rev. B* **88**, 214413 (2013).
- [60] G. Nicolas, J. Dorantes-Dávila, and G. M. Pastor, *Phys. Rev. B* **74**, 014415 (2006).
- [61] M. G. Menezes and R. B. Capaz, *Comput. Mater. Sci.* **143**, 411 (2018).
- [62] D. J. P. de Sousa, L. V. de Castro, D. R. da Costa, and J. M. Pereira, *Phys. Rev. B* **94**, 235415 (2016).
- [63] D. J. P. de Sousa, L. V. de Castro, D. R. da Costa, J. M. Pereira, and T. Low, *Phys. Rev. B* **96**, 155427 (2017).
- [64] J. S. de Sousa, M. A. Lino, D. R. da Costa, A. Chaves, J. M. Pereira, and G. A. Farias, *Phys. Rev. B* **96**, 035122 (2017).
- [65] M. A. Lino, J. S. de Sousa, D. R. da Costa, A. Chaves, J. M. Pereira, and G. A. Farias, *J. Phys. D: Appl. Phys.* **50**, 305103 (2017).
- [66] H. A. Melo, D. R. da Costa, A. Chaves, J. M. Pereira, G. A. Farias, J. S. de Sousa, and M. A. Lino, *Phys. Rev. B* **98**, 115438 (2018).
- [67] C. W. Groth, M. Wimmer, A. R. Akhmerov, and X. Waintal, *New J. Phys.* **16**, 063065 (2014).
- [68] A. Chaves, G. O. Sousa, K. Khaliji, D. R. da Costa, G. A. Farias, and T. Low, *Phys. Rev. B* **103**, 165428 (2021).
- [69] P. S. Epstein and P. Ehrenfest, *Proc. Natl. Acad. Sci. USA* **10**, 133 (1924).
- [70] V. P. Budak, D. S. Efremenko, and P. A. Smirnov, *Light Eng.* **28**, 25 (2020).